Nano Energy 41 (2017) 452–459

Contents lists available at ScienceDirect

Nano Energy

journal homepage: www.elsevier.com/locate/nanoen

Full paper

Robust three-dimensional graphene skeleton encapsulated $Na_3V_2O_2(PO_4)_2F$ nanoparticles as a high-rate and long-life cathode of sodium-ion batteries

Yameng Yin[a], Fangyu Xiong[a], Cunyuan Pei[a], Yanan Xu[a], Qinyou An[a,*], Shuangshuang Tan[a], Zechao Zhuang[a], Jinzhi Sheng[a], Qidong Li[a], Liqiang Mai[a,b,**]

[a] State Key Laboratory of Advanced Technology for Materials Synthesis and Processing, International School of Materials Science and Engineering, Wuhan University of Technology, Wuhan 430070, PR China
[b] Department of Chemistry, University of California, Berkeley, CA 94720, United States

ARTICLE INFO

Keywords:
$Na_3V_2O_2(PO_4)_2F$
Spray-drying
Graphene skeleton
Microsphere
Sodium-ion battery

ABSTRACT

$Na_3V_2O_2(PO_4)_2F$ (NVOPF) is a promising cathode material for sodium-ion batteries (SIBs) due to its high working voltage and theoretical capacity. However, the electrochemical performance is strongly impeded by its poor intrinsic electronic conductivity. Herein, we integrated the high flexible graphene sheets with NVOPF through a spray-drying method to re-construct its structure. The NVOPF nanocrystalline particles are homogeneously embedded in the high electronic conductive graphene framework. As a cathode of SIBs, the robust NVOPF/rGO microsphere composite exhibits excellent electrochemical performance: high specific capacity (127.2 mA h g^{-1}), long-term cycling stability (83.4% capacity retention at 30 C after 2000 cycles) and superior high rate performance (70.3 mA h g^{-1} at 100 C). Furthermore, the Na^+ insertion/extraction mechanism is also investigated by *in-situ* XRD and *ex-situ* HRTEM monitor technologies. This work demonstrates that the constructed 3D graphene skeleton serves as a high-efficient electronic conduction matrix and improves the electrochemical properties of electrode materials for advanced energy storage applications.

1. Introduction

Diversified and renewable energies are necessary to establish a sustainable society due to the increasingly serious environmental pollutions caused by the consumption of fossil fuels. In this regard, the development of rechargeable energy storage devices for storing intermittent sustainable energy such as solar and wind is of great importance [1,2]. Indeed, lithium-ion batteries (LIBs) are playing an increasing important role in high-efficient energy storage, however, the high cost and serious safety problems impede its further development in large scale energy storage systems [3,4]. Recently, sodium-ion batteries (SIBs) attract considerable attention and have been considered as a promising alternative to LIBs, because the inexpensive and widely distributed sodium has similar physical and chemical properties with lithium [5].

Nevertheless, compared with Li^+, Na^+ has a larger size and more sluggish diffusion kinetics. It would be a key issue to exploit an appropriate cathode material in which Na^+ can reversibly insert/extract to achieve high electrochemical performance. During past few decades, many types of cathode materials for SIBs have been thoroughly investigated, including transition metal oxides and polyanion-based compounds. The phosphate and fluorophosphates phases contain the stable phosphate-metal bonds which will reduce the risk of oxygen release [6], and the stable PO_4^{3-} polyanion can alleviate the volume change during cycles [7]. Therefore they are capable to display higher safety and better electrochemical performance compared with transition metal oxides. Among them, $Na_3V_2O_2(PO_4)_2F$ (NVOPF) as one of the most promising cathodes has been explored due to its high reversible capacity (~ 130 mA h g^{-1}) and high average discharge voltage (~ 3.8 V *vs.* Na^+/Na) [8]. However, its practical applications are limited by the poor electronic conductivity [9–13]. Goodenough et al. reported a NVOPF/graphene sandwich nanostructure which delivers a specific discharge capacity around 100.4 mA h g^{-1} at 1 C [14]; Kumar et al. combined NVOPF with multi-walled carbon nanotubes and obtained a stable capacity of 98 mA h g^{-1} at 0.1 C for 120 cycles [15]; Jin et al. fabricated NVOPF@carbon/graphene (NVOPF@C/GO), which displayed a specific capacity of 113 mA h g^{-1} at 1 C [16]; Other modification treatments, such as conductive RuO_2 coating [17] and Ru-

* Corresponding author.
** Corresponding author at: State Key Laboratory of Advanced Technology for Materials Synthesis and Processing, International School of Materials Science and Engineering, Wuhan University of Technology, Wuhan 430070, PR China.
E-mail addresses: anqinyou86@whut.edu.cn (Q. An), mlq518@whut.edu.cn (L. Mai).

http://dx.doi.org/10.1016/j.nanoen.2017.09.056
Received 14 July 2017; Received in revised form 24 September 2017; Accepted 26 September 2017
Available online 28 September 2017

doping [18] were also carried out to enhance the rate performance. Though the above-mentioned works have made good progress, the electrochemical performance is not satisfactory to meet the demand of practical applications especially at high rate charge-discharge conditions. In order to further improve its poor intrinsic electronic conductivity, we proposed to re-design the NVOPF structure by taking the advantage of high flexible graphene.

Herein, we firstly constructed a robust NVOPF/rGO microsphere composite *via* a spray-drying method and subsequent calcination process, in which the well-crystallized NVOPF particles are uniformly embedded in the three-dimensional (3D) graphene framework. The novel structure features can not only facilitate efficient electron conduction, but also maintain the morphology integrity and avoid structural degradation during the long-term cycling process. As a result, the obtained NVOPF/rGO delivers a high reversible capacity of 127.2 mA h g^{-1} at 0.2 C, shows superior cycling performance with 83.4% retention after 2000 cycles at 30 C and excellent high rate performance with a small attenuation as the cathode of SIBs. Besides, the Na^+ insertion/extraction mechanism has been investigated *via in-situ* X-ray diffraction (XRD) and *ex-situ* HRTEM technologies.

2. Experimental

2.1. Sample preparation

Firstly, ammonium metavanadate (NH_4VO_3), sodium fluoride (NaF) and ammonium dihydrogen phosphate ($NH_4H_2PO_4$) with the molar ratio of 2:3:2 dissolved in deionized water to form an even and stable solution during continuously stirring. Afterwards, appropriate graphene oxide (GO) was slowly dripped in the above solution under vigorous stirring. Then the well dispersed solution was used to prepare NVOPF/GO spherical precursor *via* a spray-drying method. Finally, the NVOPF/rGO microsphere composite was obtained after calcination process. The GO dispersion (2 mg mL^{-1}; sheet size > 500 nm) is purchased from XFNANO company. As control experiment, the pure NVOPF (denoted as S1) was synthesized through the same process without the addition of GO, which was fired at 400 °C for 5 h with a heating rate of 5 °C min^{-1}. The samples with GO were obtained under different calcination regulations: sintered at 400 °C for 5 h with a heating rate of 5 °C min^{-1} (denoted as S2); sintered at 400 °C for 5 h with a heating rate of 2 °C min^{-1} (denoted as S3) and sintered at 500 °C for 5 h with a heating rate of 2 °C min^{-1} (denoted as S4). All the burning process was carried out in the argon atmosphere.

2.2. Structure characterization

The XRD patterns and *in-situ* XRD patterns were recorded by a D8 Advance X-ray diffractometer with a Cu Kα radiation. The field emission scanning electron microscopy (FESEM) images and energy dispersive X-ray spectra (EDS) elemental mappings were collected with a JEOL-7100F microscope at an acceleration voltage of 20 kV. Transmission electron microscopy (TEM) and high resolution transmission electron microscopy (HRTEM) were carried out by using the JEM-2100F STEM/EDS microscope. Raman spectra were collected with a Renishaw INVIA micro-Raman spectroscopy system. Fourier-transform-infrared (FTIR) spectra were recorded by using a Nicolet 60-SXB IR spectrometer. The carbon content analyses were performed with CHNS elemental analyzer.

2.3. Electrochemical measurements

The cathode slurry was prepared by mixing 60 wt% of active material, 30 wt% acetylene black and 10 wt% polyvinylidene fluoride (PVDF) with an appropriate amount of N-methyl-2-pyrrolidone (NMP) as solvent. Then the blending homogeneous slurry was coated on an aluminium (Al) foil and dried at 70 °C in a vacuum oven for 12 h. The

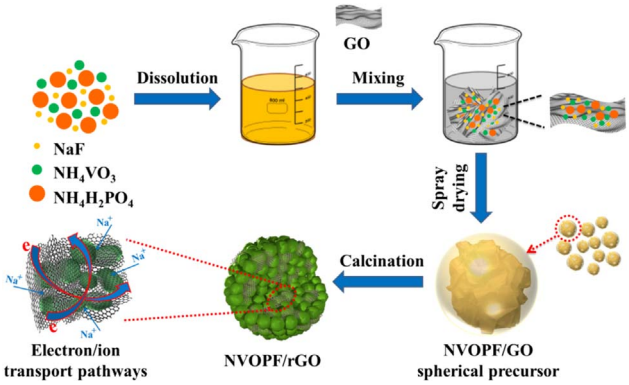

Fig. 1. The synthetic process of NVOPF/rGO microsphere composite.

electrochemical performance of each sample was evaluated by assembling 2016 coin cells which consisted of the cathode, sodium anode, glass fiber separator, and 1 M solution of $NaClO_4$ in propylene carbonate (PC) with 5% fluoroethylene carbonate (FEC) as the electrolyte in an argon-filled glove box. The galvanostatic charge-discharge tests were carried out at a voltage window of 2.5–4.5 V *versus* Na^+/Na with a multi-channel battery testing system (NEWARE). Cyclic voltammetry (CV) and electrochemical impedance spectra (EIS) were tested with an electrochemical workstation under the alternating current ranging from 0.01 Hz to 10 kHz (CHI 760D and Auto lab PGSTAT302).

3. Results and discussion

A schematic diagram of the synthetic process is shown in Fig. 1. In brief, the mixed solution is pumped into the drying chamber with a peristaltic pump and the fluid is broken into very fine mist droplets through a nozzle atomizer under a hot air pressure. The powder product is collected in cyclone separator with the rapid evaporation of moisture. Owing to the amphipathicity, GO sheets will spontaneously migrate to the surface of the solution droplets during the evaporation process [19–21]. At the same time, due to the larger lateral dimension of GO sheets compared with the NVOPF nanoparticles, the GO sheets will shrink and fold under the capillary stress [22–24]. As a result, the NVOPF nanoparticles are uniformly embedded in the constructed 3D graphene conductive network [25–27]. Most importantly, this unique structure can be well maintained after calcination. Details about solution preparation are given in the experimental section. As illustrated in Fig. 1, the constructed NVOPF/rGO microsphere can not only provide effective electron transport and fast Na^+ diffusion pathways but also alleviate stress relaxation, resulting in superior electrochemical performance.

The XRD patterns are employed to study the crystal structure of as-synthesized NVOPF/rGO (Fig. 2a). All the diffraction peaks can be readily indexed to the tetragonal NVOPF (PDF#97-041-1950, space group: I4/*mmm* [NO. 139]) [14,28,29]. No impurity reflections have been detected, which confirms the high purity of products. Moreover, because of different heating rate and calcination temperature, the intensity and full width at half maximum of all NVOPF/rGO samples are slightly different, and S4 has a higher degree of crystallinity than that of S2 and S3, which is also indicated by comparing the grain size of the NVOPF on the surface of each microsphere in Fig. S2.

Raman spectroscopy is performed to testify the surface signals of the four different samples (Fig. 2b). Owing to the existence of carbon material, all samples (except the bare NVOPF) display two broadened bands, which located at 1350 and 1580 cm^{-1} respectively, corresponding to the D-band (disorders) and G-band (graphite) [14,30–32]. Generally, the value of peak intensity ratios of D band to G band (I_D/I_G) is used to evaluate the graphitization degree of carbon materials in structure [33,34]. Apparently, the I_D/I_G among the S2-S4 are similar to

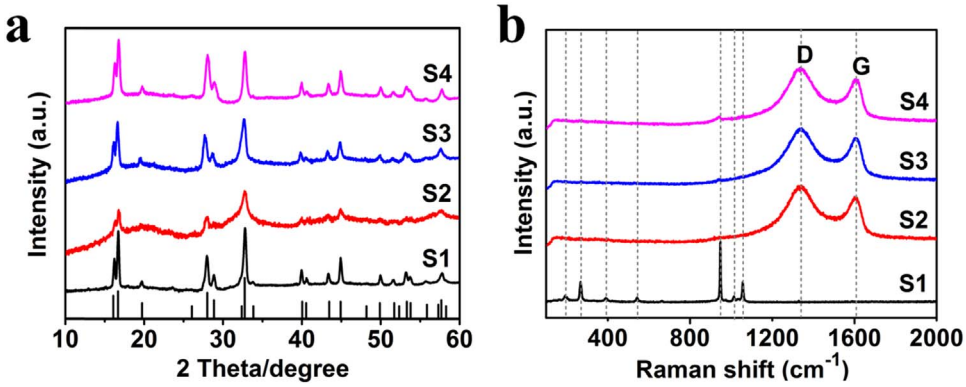

Fig. 2. (a) XRD patterns of the bare $Na_3V_2O_2(PO_4)_2F$ (S1) and $Na_3V_2O_2(PO_4)_2F$/rGO composites (S2–S4). (b) The comparison of Raman spectrum of S1–S4.

each other, which has a negligible change of values. In contrast, it is remarkable that the PO_4^{3-} signals are not detected in Raman scattering peak because the signals are masked by the tightly wrapped graphene sheets. Additionally, FTIR spectroscopy is also recorded to test the reduction level of the GO. Fig. S3 shows the FTIR spectra of graphite oxide and three annealing samples (S2-S4). The peak located at 3430 cm^{-1} can be attributed to O–H stretching vibrations of absorbed water molecules, while the band at 1384 cm^{-1} could be due to the O–H (carboxyl) bending vibration. The characteristic absorption bands of C=O (carbonyl and carboxyl) and C–O (epoxy or alkoxy) were also detected at around 1730 cm^{-1} and 1093 cm^{-1} [35]. The full deoxygenation of GO is very difficult to achieve through a single thermal annealing process, however, the great majority of oxygen-containing functional groups can be easily removed above 200 °C with appropriate time [36]. The bands of S2-S4 located at 1730 cm^{-1}, 1384 cm^{-1} and 1093 cm^{-1} are totally disappeared, demonstrating that GO was reduced and the reduction level is almost the same. Determined by the CHNS elemental analysis, the carbon contents of the S1–S4 are 0 wt%, 2.7 wt%, 2.4 wt% and 1.9 wt%, respectively.

As shown in Fig. S1, the precursors of NVOPF and NVOPF/rGO obtained from spray-drying exhibit a spherical morphology and the diameters of balls range from hundreds of nanometers to several micrometers. After annealing process, S1 is broken into pieces and cannot maintain the original architecture, while S2-S4 have no obvious structure collapse and the spherical morphology are well maintained (Fig. S2), demonstrating that the constructed 3D graphene framework has a positive effect on maintaining the structural stability. The FESEM images in Fig. 3a shows that the morphology of S4 is spherical and the higher magnified insert image presents that each microsphere is assembled by irregular NVOPF nanoparticles and rGO sheets. In order to further check the existence and distribution of every element (Na, V, P, O, F, C) in the microsphere, EDS mapping is performed. In Fig. 3a, we can see that every element is homogeneously distributed throughout the entire microsphere. Furthermore, TEM observation is performed to confirm the detailed internal microstructures of the as-prepared S4. Fig. 3b and c show a direct look on the morphology, corresponding well with the SEM images. Owing to the tightly binding of irregular nanoparticles which wrapped by graphene sheets, the NVOPF/rGO microsphere composite is confirmed to be a solid structure. In the edge of a single sphere, the HRTEM image (Fig. 3d) clearly displays the well-defined graphene sheets and the lattice fringes of 0.53 nm, which corresponding well with the (002) crystal plane of the NVOPF. In order to investigate the microstructure of graphene framework, the NVOPF was etched from the NVOPF/rGO by hydrofluoric acid. After etching, a spitball-like carbon skeleton can be obtained (Fig. 3e). Obviously, only carbon can be detected by EDS mapping.

The electrochemical performance of the four samples as cathode materials for SIBs are measured in half cell with a voltage window of 2.5–4.5 V *vs.* Na^+/Na. Firstly, CV was measured at a scan rate of 0.1 mV s^{-1} to identify the activity of the vanadium redox couple. The CV curves of S4 are shown in Fig. 4a. Owing to the reversible intercalation of Na^+ into Na(1) and Na(2) sites in the structure, two pair of redox peaks located at around 3.65/3.60 V and 4.07/4.00 V have been observed, which is corresponding to the activity of V^{4+}/V^{5+} couple. Besides, the CV plots of other three samples are shown in Fig. S4. It can be found that the S4 has a smaller polarization and sharper peaks, reflecting better electrochemical kinetics. The cycle behaviors of the bare NVOPF and various NVOPF/rGO samples in non-aqueous electrolytes are studied at low current density (0.5 C). As shown in Fig. 4b, the S4 displays an initial discharge capacity of 120.4 mA h g^{-1}, which is higher than that of S3, S2 and S1 (101.6 mA h g^{-1}, 69.7 mA h g^{-1} and 25.4 mA h g^{-1}, respectively). Moreover, S4 exhibits an optimum cycling stability, which maintains a discharge capacity of 107.9 mA h g^{-1} after 200 cycles, corresponding to 89.7% of the initial discharge capacity, which is higher than that of S3, S2 and S1 (70.7%, 66.6% and 87.9%, respectively). The corresponding initial charge-discharge curves of the four samples at 0.5 C are shown in Fig. 4c. Two plateaus can be observed at ~ 4.0 V and ~ 3.6 V in the discharge curves, respectively, coinciding with the CV test results. Besides, the charge/discharge curves of S4 in different cycles at 0.5 C is shown in Fig. S5. The rate performance of the four samples has been investigated at various charge-discharge current densities (Fig. 4d). Obviously, with the increasing of current density, the S4 exhibits higher capacity and smaller capacity decay than S1–S3. At the current of 0.2 C and 20 C, the S4 delivers discharge capacities of 127.2 and 89.2 mA h g^{-1}, respectively. When the test current returns to 0.2 C, the discharge capacity recovers to 123.1 mA h g^{-1}, and the corresponding capacity retention is 96.8%. The galvanostatic charge-discharge curves of S4 at different rates from 0.2 to 20 C are displayed in Fig. 4e, which shows a small polarization. In sharp contrast, the rate performance of S4 is obviously improved , the main reasons are as follows: (1) 3D graphene conductive network greatly enhances the electronic conductivity of the material and maintains the stability of structure in the cycling process; (2) with the increasing of calcination time and temperature, the material has been better crystallized, which has a positive effect on improving the ions mobility.

The EIS measurements of the assembled half cells after three cycles were carried out to investigate the electrochemical reaction kinetics. The Nyquist plots (Fig. 4f) show a semicircle in the medium-frequency region and a slanted line in the low frequency range. The diameter of semicircle represents the value of charge transfer resistance (R_{ct}) between the electrolyte and electrode. All graphene modified products (S2, S3 and S4) are smaller than the bare NVOPF (S1), indicating that the 3D graphene network not only enhances the charge transfer kinetics but also provides more efficient electron/ion transport pathways [13,37]. Moreover, the R_{ct} of S4 is much smaller than S2 and S3, demonstrating that the improved crystallinity and increased of grain size will enhance the contact between NVOPF nanoparticles and graphene matrices, which could promote the rapid diffusion of ions and electrons [38,39].

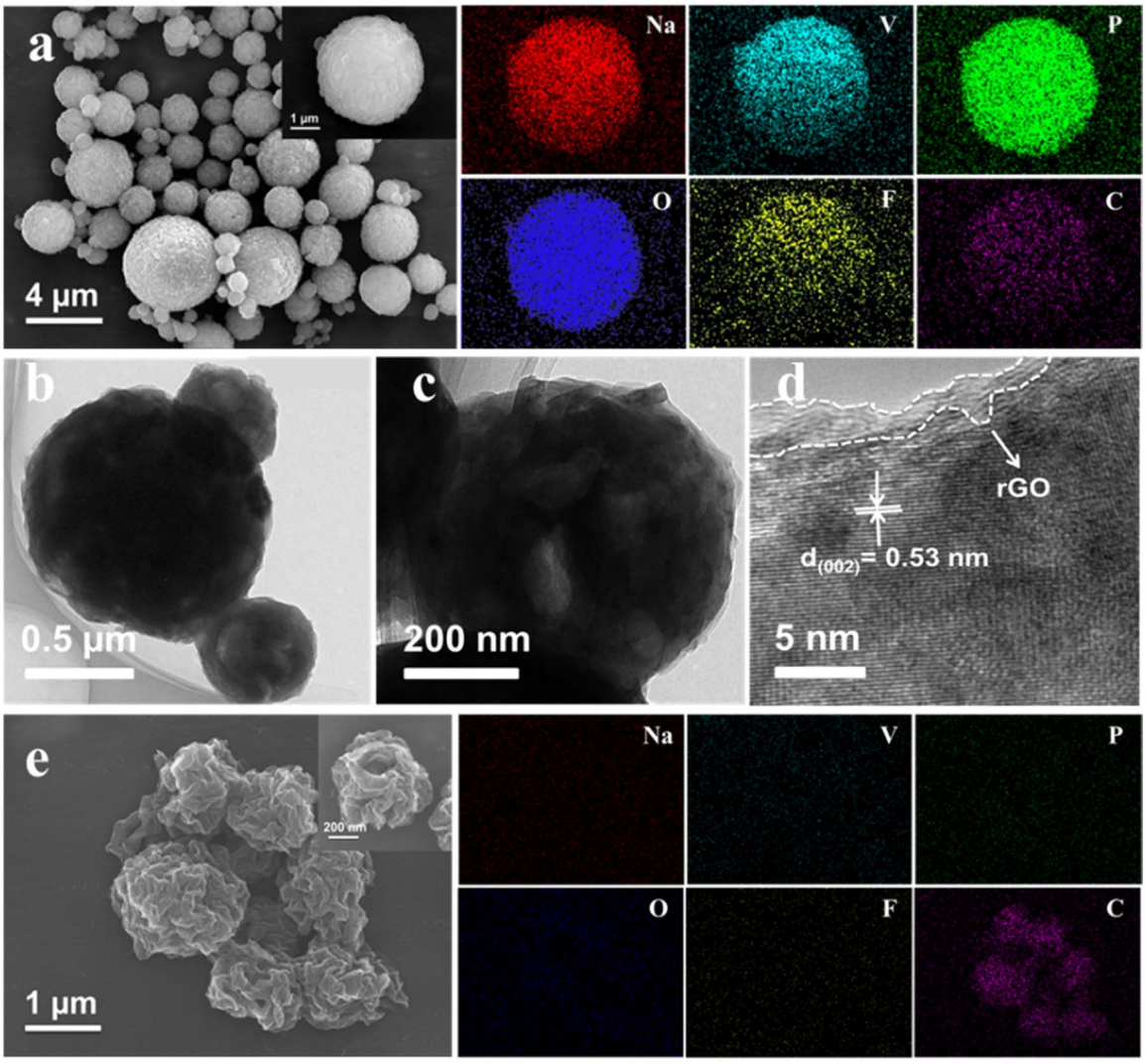

Fig. 3. (a) FESEM images and EDS-mapping of S4. (b–d) TEM and HRTEM images. (e) The FESEM images and EDS-mapping of 3D graphene skeleton.

According to the above results, the S4 displays the best electrochemical performance among the four samples. The high rate performance is further explored at various specific currents ranging from 10 to 100 C (Fig. 5a). When the current rate is increased to 30, 50, 60 and 80 C, the discharge capacities are 87.2, 83.6, 81.4 and 76.3 mA h g^{-1}, respectively. Even under an extremely high rate of 100 C, a capacity of 70.3 mA h g^{-1} is still obtained, the corresponding charge/discharge process can be finished in 24 s. When the current density is turned back to 10 C, the reversible capacity can be returned to 90.6 mA h g^{-1}, exhibiting a remarkable capacity recovery. The whole rate performance chart shows a slight decline with the current rate gradually increasing, which could be ascribed to the effect of graphene network (enhancing the electronic conductivity and accelerating Na^+ transport). The corresponding charge-discharge curves at different rates are shown in Fig. 5b. In order to make a comparison with published references [14–18], the specific values are shown in Table S1. As shown in Fig. 5c, the designed NVOPF/rGO microsphere composite has a distinct advantage in the high rate cycle stability but with the lowest carbon contents (1.9 wt%) and relatively wide working potential range (2.5–4.5 V). These results show that the 3D graphene framework supported NVOPF microsphere has great potential application in large scale energy storage devices. In addition, the long-term cycling performance of NVOPF/rGO (S4) at 30 C and corresponding charge-discharge curves are shown in Fig. 5d and e. The NVOPF/rGO cathode delivers an initial reversible discharge capacity of 87.2 mA h g^{-1} and retains the capacity of 72.7 mA h g^{-1} after 2000 cycles, the capacity retention is 83.4%. The Coulombic efficiency averages 99.7%, demonstrating that the Na^+ insertion/extraction process is highly reversible. Moreover, the SEM images before and after 2000 cycles at 30 C are shown in Fig. S6. It can be seen that there is no obvious change in the morphology of electrode and the initial spherical structure can be well maintained, which indicates that the robust 3D graphene skeleton is highly effective in shortening electronic/ion diffusion pathways and buffering the volume change upon cycling.

To better reveal the Na^+ insertion/extraction mechanism in the electrochemical process of NVOPF/rGO as the cathode for SIBs, the time-resolved *in-situ* XRD technique is performed. The *in-situ* XRD patterns of S4 during the first two cycles and the corresponding voltage curves are displayed in Fig. 6a. It can be directly observed that the diffraction peaks centered at 28.0°, 32.6° and 40.2° (corresponds to the planes of (200), (202) and (220), respectively) gradually shift towards higher angles during the initial charging process. Subsequently, all the diffraction patterns shift back to their original positions in the following discharging process. In addition, the discharge plateaus are in good agreement with charge plateaus, and the same trend also come out in the second cycle, reflecting a reversible insertion/extraction of Na^+ and good crystal structure stability. As shown in Fig. 6b, there are two kinds of Na^+ sites in structure which are separated by the coordination environment: the Na(1) site is coordinated by six O and one F, but the Na (2) site only with six O. The layer unit is composed of [VO_5F]

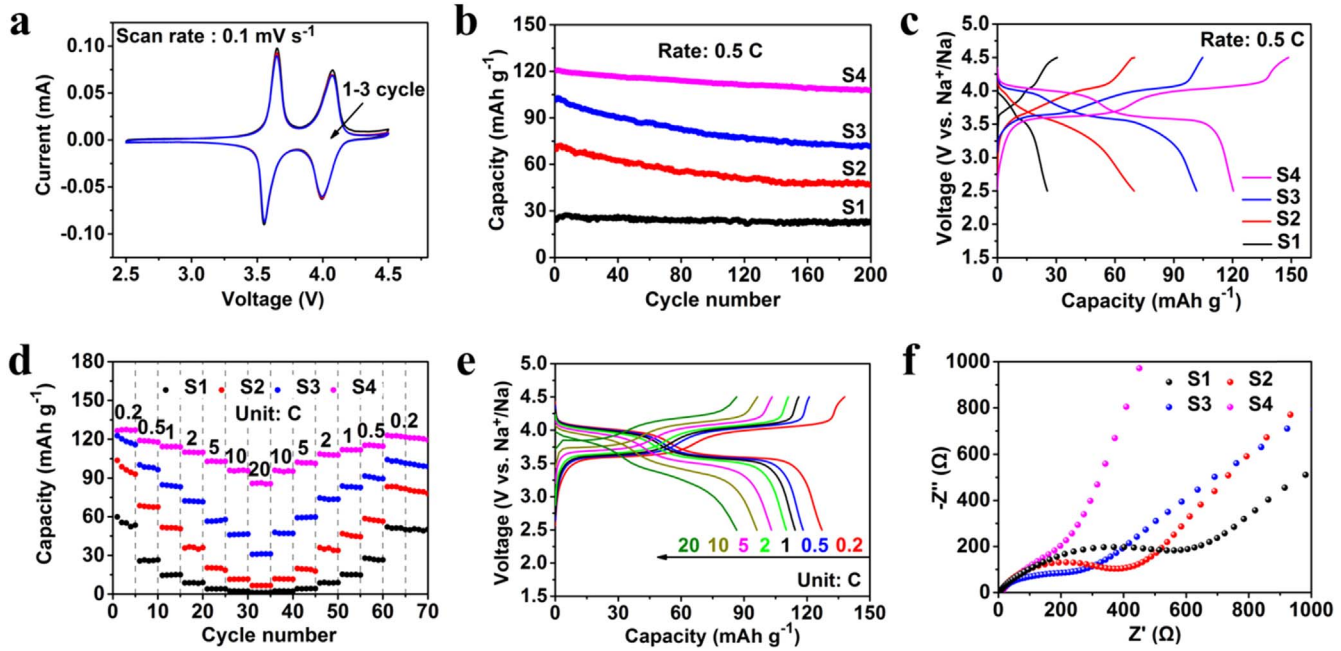

Fig. 4. The electrochemical performance of the NVOPF-based materials. (a) The CV curves of S4 in first three cycles at a scan rate of 0.1 mV s^{-1}. (b, c) Cycle performances and the initial charge-discharge curves of S1–S4 at the current density of 0.5 C. (d) The comparison of rate performance. (e) The corresponding galvanostatic charge-discharge profiles of S4 cycled at different current rates from 0.2 to 20 C. (f) The Nyquist plots of the fully discharged S1–S4 after three cycles at 0.5 C.

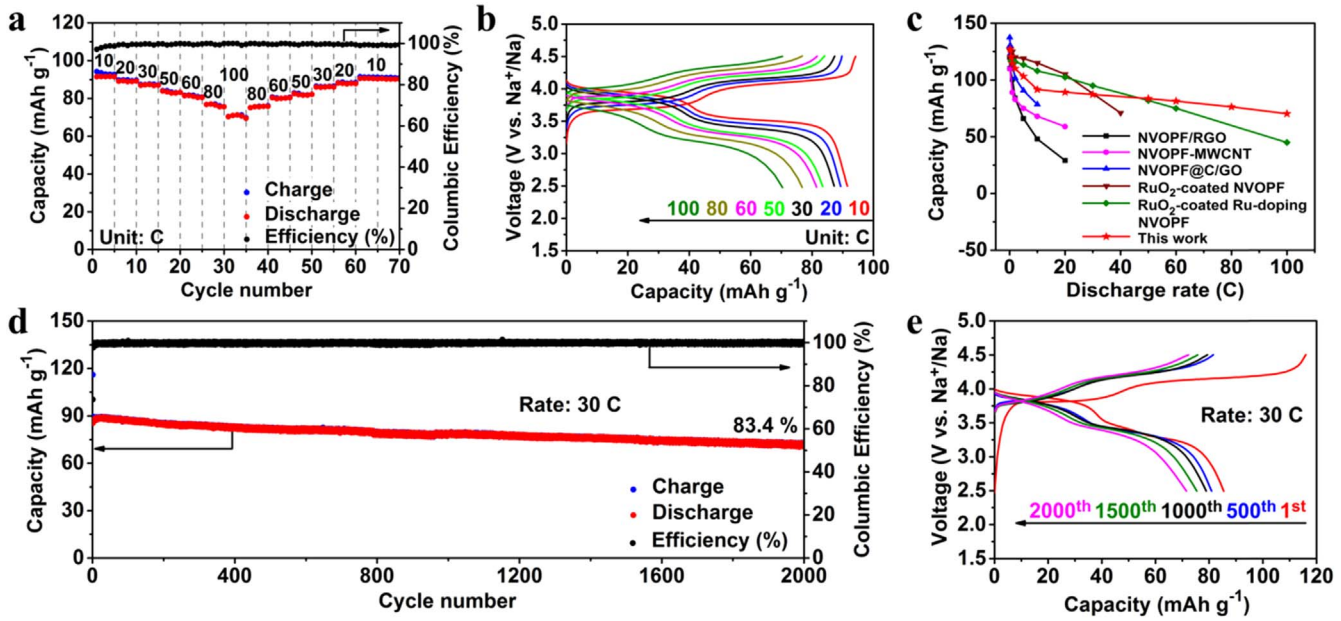

Fig. 5. The electrochemical properties of the NVOPF/rGO (S4) in the potential window range from 2.5 to 4.5 V. (a, b) High rate performance and corresponding charge-discharge curves. (c) The comparison of rate performance with recent literatures (NVOPF/RGO;[14] NVOPF-MWCNT;[15] NVOPF@C/GO;[16] RuO_2-coated NVOPF;[17] RuO_2-coated Ru-doping NVOPF[18]). (d) The long-term cycle performance of S4 at 30 C. (e) The corresponding charge-discharge curves in different cycles.

octahedrons and $[PO_4]$ tetrahedrons by sharing one oxygen atom. With these, Na(1) and Na(2) are placed like a circle geometry in the (*ab*) plane with the disordered Na^+ ions (Fig. 6c). At the same time, two $[VO_5F]$ octahedrons are united by one fluorine atom between layers in the crystal structure as shown in Fig. 6d. The broad channel in the open framework structure is conducive to the rapid diffusion of sodium ions during the charge and discharge processes. With the migration of Na^+ from two different sites, only the shift of peaks can be observed and no new peaks appeared, confirming that the (de)sodiation procedure of NVOPF/rGO is a typical two-step single solid solution reaction as Eqs. (1) and (2) [16,40–43].

$$\text{Plateau I}: Na_3V_2O_2(PO_4)_2F \leftrightarrow Na_xV_2O_2(PO_4)_2F + xNa^+ + xe^-(2 \le x \le 3) \quad (1)$$

$$\text{Plateau II}: Na_2V_2O_2(PO_4)_2F \leftrightarrow Na_xV_2O_2(PO_4)_2F + xNa^+ + xe^-(1 \le x \le 2) \quad (2)$$

Sauvage et al. have demonstrated that there is a short distances (1.497 Å) between Na(1) and Na(2) sites, which means that the two sites cannot be occupied simultaneously [44]. Meanwhile, the binding energy of Na(1) (4.70 eV) in the dilute limit is higher than that of Na(2) (4.62 eV) due to the existence of Na–F, indicating that Na(1) is more stable than Na(2) [45]. Thus, the most likely crystal structure of

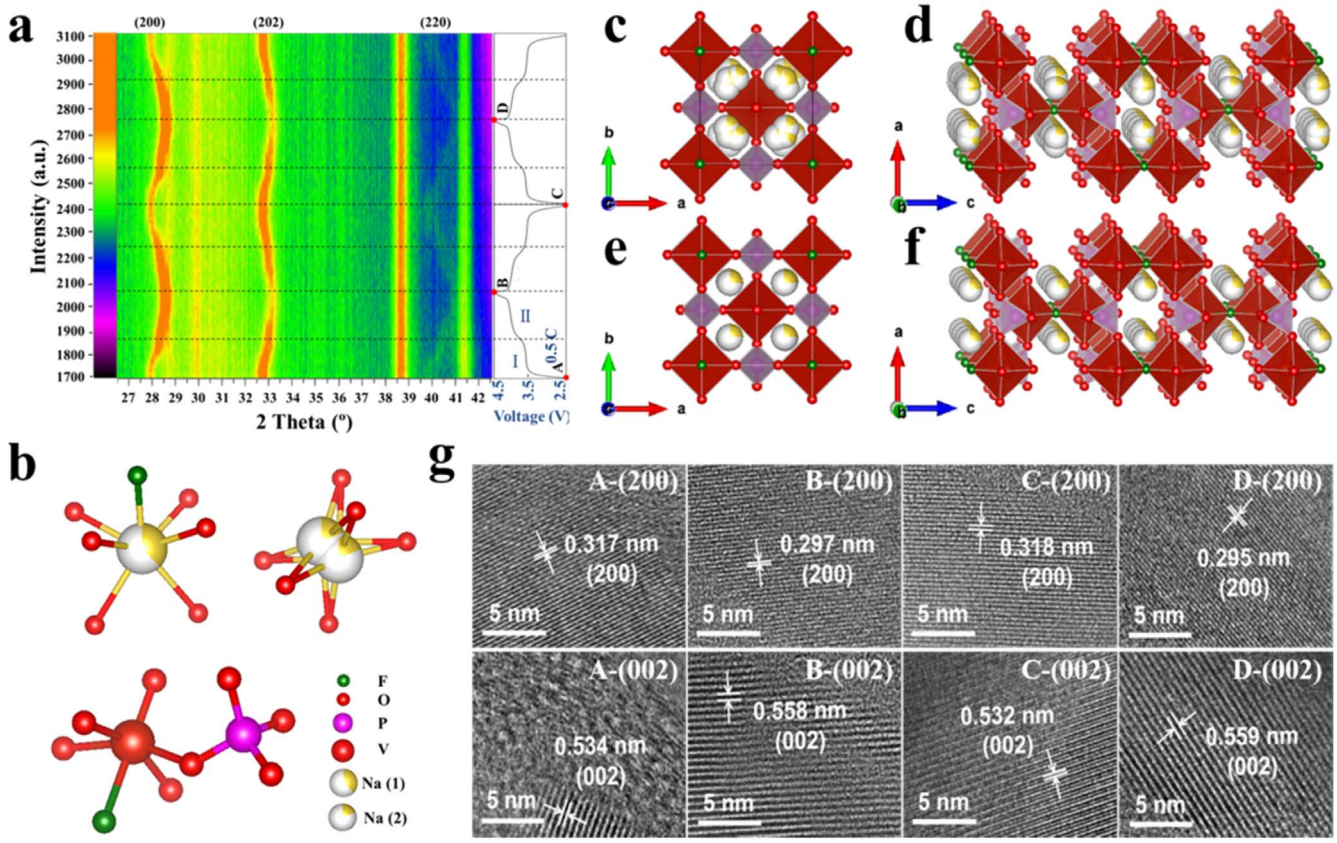

Fig. 6. (a) *In-situ* XRD patterns of S4 and the corresponding charge/discharge curves during the first two cycles in the potential of 2.5–4.5 V at 0.5 C. (b) A schematic illustration of the Na^+, V^{4+} and P^{5+} coordination environment. (c, d) The original crystal structure representation of $Na_3V_2O_2(PO_4)_2F$ in the (*ab*) and (*ac*) plane. (e, f) The most stable structure schematic diagrams of $NaV_2O_2(PO_4)_2F$ in the (*ab*) and (*ac*) plane. (g) *Ex-situ* HRTEM images of the electrode at four different states (A is the initial state; B is the full charge state in the first cycle; C is the full discharge state in the first cycle and D is the full state of charge in the second cycle).

$NaV_2O_2(PO_4)_2F$ is displayed in Fig. 6e and f. Additionally, to grasp further insight into the Na^+ storage mechanism, the *ex-situ* HRTEM images of the electrode at different charge/discharge states were collected. Fig. 6g shows obvious changes of the lattice spacing of (200) and (002) during the de/insertion of Na^+. From state A to B, two sodium ions gradually extract from the structure, resulting in the decrease/increase of the interlayer spacing (d_{200})/(d_{002}), indicating the decrease in *a* parameter and increase in *c*. On the contrary, the d_{200} and d_{002} gradually return to their original values when fully discharged to 2.5 V, reflecting the reversibility of structure, which fits well with the *in-situ* XRD results.

4. Conclusion

In summary, a robust 3D graphene framework supported NVOPF/rGO microsphere composite is successfully prepared for the first time through a spray-drying method and followed calcination procedure. The enhanced charge transfer kinetics, bicontinuous electron/Na^+ ion transport pathways and superior mechanical stability based on graphene network ensure the highly reversible (de)intercalation of Na^+. The obtained NVOPF/rGO exhibits high capacity (120.4 mA h g^{-1} at 0.5 C), outstanding high-rate capability (70.3 mA h g^{-1} at 100 C) and excellent ultra-long cycling stability (83.4 % after 2000 cycles at 30 C). Besides, a two-step single solid solution reaction mechanism basing on the repeating insertion/extraction of two Na^+ is also observed by *in-situ* XRD and *ex-situ* HRTEM. Such excellent results demonstrate that the synthesized NVOPF/rGO microsphere composite is a very promising cathode material for the high performance SIBs. Moreover, we believe that the facile and effective synthesis strategy will provide a new direction to optimize the electrochemical performance and can also be further extended to other materials, which will inspire the successful development of large scale energy storage applications in future.

Acknowledgements

This work was supported by the National Key Research and Development Program of China (2016YFA0202603), the National Basic Research Program of China (2013CB934103), the National Natural Science Foundation of China (51602239), the Hubei Provincial Natural Science Foundation of China (2016CFB267), and the Fundamental Research Funds for the Central Universities (WUT: 2016III003, 2016IVA090, 2017III005, 2017-zy-008), Prof. Liqiang Mai gratefully acknowledged financial support from China Scholarship Council (No. 201606955096).

Appendix A. Supplementary material

Supplementary data associated with this article can be found in the online version at http://dx.doi.org/10.1016/j.nanoen.2017.09.056.

References

[1] H.S. Kim, T.S. Arthur, G.D. Allred, J. Zajicek, J.G. Newman, A.E. Rodnyansky, A.G. Oliver, W.C. Boggess, J. Muldoon, Nat. Commun. 2 (2011) 427–432.
[2] Y.U. Park, D.H. Seo, H.S. Kwon, B. Kim, J. Kim, H. Kim, I. Kim, H.I. Yoo, K. Kang, J. Am. Chem. Soc. 135 (2013) 13870–13878.
[3] Q. An, F. Xiong, Q. Wei, J. Sheng, L. He, D. Ma, Y. Yao, L. Mai, Adv. Energy Mater. 5 (2015) 1963–1972.
[4] Y. Yu, J. Liu, L. Yu, C. Wu, Y. Wen, K. Yin, F.K. Chiang, R. Hu, J. Liu, L. Sun, Nano Lett. 17 (2017) 2034–2042.
[5] M.H. Han, E. Gonzalo, G. Singh, T. Rojo, Energy Environ. Sci. 8 (2014) 81–102.
[6] R.K.B. Gover, N.D. Withers, S. Allen, R.L. Withers, J.S.O. Evans, J.Solid State Chem. 166 (2002) 42–48.

[7] J. Zheng, Y. Han, B. Zhang, C. Shen, L. Ming, X. Ou, J. Zhang, ACS Appl. Mater. Interfaces 6 (2014) 6223–6226.
[8] P. Serras Malillos, Int. J. Cancer 56 (2014) 269–274.
[9] H.B. Lung-Hao, F.Y. Wu, C.T. Lin, A.N. Khlobystov, L.J. Li, Nat. Commun. 4 (2013) 1687–1693.
[10] Y. Kim, Y. Park, A. Choi, N.S. Choi, J. Kim, J. Lee, J.H. Ryu, S.M. Oh, K.T. Lee, Adv. Mater. 25 (2013) 23045–23049.
[11] D. Su, H.-J. Ahn, G. Wang, Chem. Commun. 49 (2013) 3131–3133.
[12] Y. Wen, K. He, Y. Zhu, F. Han, Y. Xu, I. Matsuda, Y. Ishii, J. Cumings, C. Wang, Nat. Commun. 5 (2014) 4033–4042.
[13] J.Z. Guo, X.L. Wu, F. Wan, J. Wang, X.H. Zhang, R.S. Wang, Chem. – Eur. J. 21 (2015) 17371–17378.
[14] M. Xu, L. Wang, X. Zhao, J. Song, H. Xie, Y. Lu, J.B. Goodenough, Phys. Chem. Chem. Phys. 15 (2013) 13032–13037.
[15] P.R. Kumar, Y.H. Jung, J.E. Wang, D.K. Kim, J. Power Sources 324 (2016) 421–427.
[16] H. Jin, J. Dong, E. Uchaker, Q. Zhang, X. Zhou, S. Hou, J. Li, G. Cao, J. Mater. Chem. A 3 (2015) 17563–17568.
[17] M. Peng, B. Li, H. Yan, D. Zhang, X. Wang, D. Xia, G. Guo, Angew. Chem. 127 (2015) 6452–6456.
[18] M. Peng, D. Zhang, L. Zheng, X. Wang, Y. Lin, D. Xia, Y. Sun, G. Guo, Nano Energy 31 (2017) 64–73.
[19] Y.S. He, P. Gao, J. Chen, X. Yang, X.Z. Liao, J. Yang, Z.F. Ma, RSC Adv. 1 (2011) 958–960.
[20] H. Tang, G.J. Ehlert, Y. Lin, H.A. Sodano, Nano Lett. 12 (2012) 84–90.
[21] H.D. Jang, S.K. Kim, H. Chang, J.-W. Choi, J. Luo, J. Huang, Aerosol Sci. Technol. 47 (2013) 93–98.
[22] H. Chen, M.B. Müller, K.J. Gilmore, G.G. Wallace, D. Li, Adv. Mater. 20 (2013) 3557–3561.
[23] J. Kim, L.J. Cote, F. Kim, J. Huang, J. Am. Chem. Soc. 132 (2009) 260–267.
[24] J. Luo, X. Zhao, J. Wu, H.D. Jang, H.H. Kung, J. Huang, J. Phys. Chem. Lett. 3 (2012) 1824–1829.
[25] Z.D. Huang, B. Zhang, S.W. Oh, Q.B. Zheng, X.Y. Lin, N. Yousefi, J.K. Kim, J. Mater. Chem. 22 (2012) 3591–3599.
[26] T.J. Booth, P. Blake, R.R. Nair, D. Jiang, E.W. Hill, U. Bangert, A. Bleloch, M. Gass, K.S. Novoselov, M.I. Katsnelson, Nano Lett. 8 (2008) 2442–2446.
[27] G.W. Zhou, J. Wang, P. Gao, X. Yang, Y.S. He, X.Z. Liao, J. Yang, Z.F. Ma, Ind. Eng. Chem. Res. 52 (2013) 1197–1204.
[28] N. Sharma, P. Serras, V. Palomares, H.E.A. Brand, J. Alonso, P. Kubiak, M.L. Fdezgubieda, T. Rojo, Chem. Mater. 26 (2014) 3391–3402.
[29] W. Massa, O.V. Yakubovich, O.V. Dimitrova, Solid State Sci. 4 (2002) 495–501.
[30] C. Zhu, K. Song, P.A. van Aken, J. Maier, Y. Yu, Nano Lett. 14 (2014) 2175–2180.
[31] X. Tang, S.S. Jan, Y. Qian, H. Xia, J. Ni, S.V. Savilov, S.M. Aldoshin, Sci. Rep. 5 (2015) 11958–11967.
[32] N. Zhang, X. Han, Y. Liu, X. Hu, Q. Zhao, J. Chen, Adv. Energy Mater. 5 (2014) 1123–1129.
[33] S. Singh, S. Mitra, Electrochim. Acta 123 (2014) 378–386.
[34] Z.S. Wu, W. Ren, L. Gao, J. Zhao, Z. Chen, B. Liu, D. Tang, B. Yu, C. Jiang, H.M. Cheng, ACS Nano 3 (2010) 411–417.
[35] H. Guo, X. Wang, Q. Qian, F. Wang, X. Xia, ACS Nano 3 (2009) 2653–2659.
[36] S. Pei, H. Cheng, Carbon 50 (2012) 3210–3228.
[37] H. Zhang, H. Tao, Y. Jiang, Z. Jiao, M. Wu, B. Zhao, J. Power Sources 195 (2010) 2950–2955.
[38] Y. Xu, Q. Wei, C. Xu, Q. Li, Q. An, P. Zhang, J. Sheng, L. Zhou, L. Mai, Adv. Energy Mater. 6 (2016) 389–397.
[39] B. Li, N. Zhang, K. Sun, Small 10 (2014) 2039–2046.
[40] V. Palomares, M. Casascabanas, E. Castillomartínez, M.H. Han, T. Rojo, Energy Environ. Sci. 6 (2013) 2312–2337.
[41] G. Deng, D. Chao, Y. Guo, Z. Cheng, H. Wang, S.V. Savilow, J. Lin, Z.X. Sheng, Energy Storage Mater. 5 (2016) 198–204.
[42] P. Serras, V. Palomares, J. Alonso, N. Sharma, J.M.L.D. Amo, P. Kubiak, M.L. Fdez-Gubieda, T. Rojo, Chem. Mater. 25 (2013) 4917–4925.
[43] A.A. Tsirlin, R. Nath, A.M. Abakumov, Y. Furukawa, D.C. Johnston, M. Hemmida, H.A.K.V. Nidda, A. Loidl, C. Geibel, H. Rosner, Phys. Rev. B: Condens. Matter 84 (2011) 44 – 44.
[44] F. Sauvage, E. Quarez, J.M. Tarascon, E. Baudrin, ChemInform 38 (2007) 1215–1221.
[45] M. Xu, P. Xiao, S. Stauffer, J. Song, G. Henkelman, J.B. Goodenough, Chem. Mater. 26 (2014) 3087–3097.

Yameng Yin received her B.S. degree in Department of Materials Science and Engineering from Hebei University of Architecture in 2014. She is currently working toward the Ph.D. degree and her current research focuses on nanomaterials for energy storage materials and devices.

Fangyu Xiong received his B.S. degree in Material Physics and Chemistry from Wuhan University of Technology in 2016. He is currently working toward the Ph.D. degree and his current research interests focuses on electrode materials for emerging energy storage devices.

Cunyuan Pei received his B.S. degree in Department of Materials Science and Engineering from Hebei University of Architecture in 2014. He is currently working toward the Ph.D. degree and focuses on nanomaterials and electrolytes for magnesium ion battery.

Yanan Xu received his B.S. degree in Department of Materials Science and Engineering from Wuhan Uni-versity of Technology in 2013. He is currently working toward the Ph.D. degree. His current research involves the nanomaterials achieving high energy density and power density for lithiumion battery, sodium ion battery and magnesium ion battery.

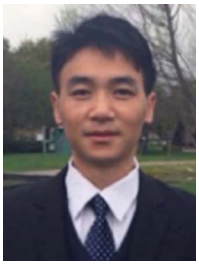

Qinyou An is Associate Professor of Materials Science and Engineering at Wuhan University of Technology (WUT). He received his Ph.D. degree from WUT in 2014. He carried out his postdoctoral research in the laboratory of Prof. Yan Yao at the University of Houston in 2014–2015. Currently, his research interest includes energy storage materials and devices.

Shuangshuang Tan received his B.S. degree in Material Science and Engineering from Wuhan University of Technology in 2016. He is currently working toward the Ph.D. degree and his current research focuses on the energy storage materials and devices.

Zechao Zhuang received his Master of Engineering degree from Fujian Normal University in 2015. He is currently a Ph.D. candidate under supervision of Prof. Liang Zhou and Prof. Liqiang Mai in Wuhan University of Technology. His research interests mainly focus on rational design of high-efficient electrocatalysts.

Jinzhi Sheng received his M.S. degree in Materials Engineering from Wuhan University of Technology in 2015. He is currently working toward the Ph.D. degree and his current research focuses on the energy storage materials and devices.

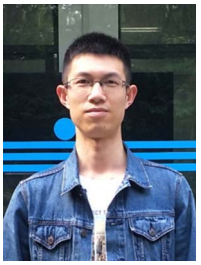

Qidong Li received his M.S. degree in Materials Engineering from Wuhan University of Technology in 2015. He is currently working toward the Ph.D. degree and his current research focuses on the energy storage materials and devices.

Liqiang Mai is Chair Professor of Materials Science and Engineering at Wuhan University of Technology (WUT). He is Cheung Kong Scholar Chair Professor and the winner of the National Natural Science Fund for Distinguished Young Scholars. His current research interests focus on new nanomaterials for electrochemical energy storage and micro/nano energy devices. He received his Ph.D. degree from WUT in 2004. He carried out his postdoctoral research in the laboratory of Prof. Zhonglin Wang at Georgia Institute of Technology in 2006–2007 and worked as advanced research scholar in the laboratory of Prof. Charles M. Lieber at Harvard University in 2008–2011. He worked as advanced research scholar in the laboratory of Prof. Peidong Yang at University of California, Berkeley in 2017.